



Non-precious $\text{Co}_3\text{O}_4\text{-TiO}_2/\text{Ti}$ cathode based electrocatalytic nitrate reduction: Preparation, performance and mechanism

Jianan Gao^a, Bo Jiang^{a,b,*}, Congcong Ni^a, Yuanfeng Qi^a, Yanqing Zhang^a, Nihal Oturan^b, Mehmet A. Oturan^{b,**}

^a School of Environmental and Municipal Engineering, Qingdao University of Technology, Qingdao 266033, PR China

^b Université Paris-Est, Laboratoire Géomatériaux et Environnement, (EA 4508), UPEM, 5 Bd Descartes, Université Paris-Est, 77454 Marne-la-Vallée, Cedex 2, France

ARTICLE INFO

Keywords:

Nitrate reduction
Electrocatalysis
 $\text{Co}_3\text{O}_4\text{-TiO}_2/\text{Ti}$ cathode
 $\text{Co}^{3+}/\text{Co}^{2+}$ redox couple
Non-precious catalyst

ABSTRACT

The presence of high nitrate (NO_3^-) concentration in natural water constitutes a serious issue to the environment and human health. Therefore, the development of low-cost, stable non-precious metal catalysts is imminent for efficient NO_3^- reduction. In this study, we prepared a $\text{Co}_3\text{O}_4\text{-TiO}_2/\text{Ti}$ cathode via combining sol-gel and calcination methods and evaluated its performance for electrocatalytic NO_3^- reduction. The dispersion of the Co_3O_4 catalyst particles was improved by the addition of PVP to the coating liquid. The presence of anatase could effectively stabilize Co_3O_4 and prevent the releasing of toxic Co ions into the solution. The $\text{Co}_3\text{O}_4\text{-TiO}_2/\text{Ti}$ cathode with the optimized performance for NO_3^- reduction could be prepared by four times coating at calcination temperature of 500 °C. The electrocatalytic reduction of NO_3^- was negligibly impacted by solution pH in the range of 3.0–9.0, while it could be facilitated by elevating the current density from 2.5 to 25 mA cm^{-2} . Ammonium ions were the main final NO_3^- reduction product, and the presence of Cl^- was capable to oxidize ammonium ions to N_2 due to the electrochemical production of reactive chlorine species. The electrochemical analyses, scavenging experiments and density functional theory calculations collectively confirm that NO_3^- reduction was mainly induced by the $\text{Co}^{2+}\text{-Co}^{3+}\text{-Co}^{2+}$ redox process instead of being directly resulted from the electrons generated at the cathode. Unlike noble metal (e.g., Pd and Ag) based catalytic reaction systems, in the present Co_3O_4 mediated electrocatalytic reaction process, atomic H^* would more favorably turn to H_2 by Heyrovsky and Tafel routes and therefore contributed marginally to the NO_3^- reduction. Generally, this study provided a new paradigm for designing the stable and cost-effective cathode for NO_3^- reduction.

1. Introduction

In water, nitrate (NO_3^-) is considered an underlying hazardous material that is derived from various sources including the feedlot runoff, the excessive use of nitrogen fertilizer and natural degradation of pollutants [1]. The presence of NO_3^- in drinking water can cause serious health problems such as the cancers, liver damage and blue baby syndrome due to its transformation product, i.e. nitrite anions (NO_2^-) [2]. To diminish this potential health risk, the concentration limit for NO_3^- in drinking water is set at 10 and 11.3 ppm by the United States EPA and the European Drinking Water Directive, respectively [3,4]. In this regard, the removal technologies of NO_3^- are imperative demands in populated regions.

Physicochemical treatments such as electrodialysis, ion exchange

and reverse osmosis are the most common technologies for NO_3^- removal from water [5], but the post-treatments are still needed to address the concentrated solutions produced in these methods. Although biological denitrification can gradually convert NO_3^- to N_2 [6], it is a time-consuming process and its performance is strongly impacted by the variable conditions, such as dissolved oxygen and temperature. Recently, zero valent metals (e.g. iron [7], aluminum [8], and magnesium [9]) based stoichiometrically chemical reduction of NO_3^- has been increasingly explored. Unfortunately, the flexibility of this strategy is greatly confined by the formation of inert oxide surface, deteriorating the electron transfer efficiency, and the inevitable production of secondary solid sludge. More recently, some catalytic hydrogenation processes with the combined noble/promoting metals (e.g., Pd/Cu and Pd/Fe) have been proposed for NO_3^- reduction

* Corresponding author at: School of Environmental and Municipal Engineering, Qingdao University of Technology, Qingdao 266033, P.R. China.

** Corresponding author at: Université Paris-Est, Laboratoire Géomatériaux et Environnement, (EA 4508), UPEM, 5 Bd Descartes, Université Paris-Est, 77454 Marne-la-Vallée, Cedex 2, France.

E-mail addresses: bjiang86upc@163.com (B. Jiang), Mehmet.Oturan@univ-paris-est.fr (M.A. Oturan).

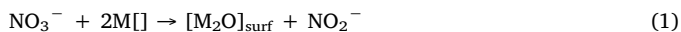
<https://doi.org/10.1016/j.apcatb.2019.05.016>

Received 7 March 2019; Received in revised form 27 April 2019; Accepted 2 May 2019

Available online 03 May 2019

0926-3373/ © 2019 Elsevier B.V. All rights reserved.

[10,11]. In these processes, the reduction of NO_3^- is mainly initiated by promoter metal (Eq. (1)) with the formation of NO_2^- , and the subsequent reduction process is gradually achieved by the noble metal activated hydrogen (Eq. (2)) [12]. However, catalytic hydrogenation reduction requires H_2 as a reducing agent or electron donor, and there are safety hazards in the transport and use of H_2 , which greatly limits its industrial application potential [13].



Considering the advantages of self-produced hydrogen, environmental compatibility and ambient operating conditions, electrocatalysis has been regarded as a promising method for denitrification [14], in which the reduction of NO_3^- can be obtained by either a direct or an indirect pathway at the cathode surface. Direct reduction of NO_3^- is initiated by the electron tunneling or generation of chemisorbed complex between the NO_3^- and cathode whereas in the indirect pathway, NO_3^- is reduced by a surface-adsorbed atom H^* , which is produced from the reduction of protons by electron via the Volmer process [15]. Specially, Pd-based catalysts have recently been distinguished mainly because of their potential to electrochemically reduce oxyanion contaminants in water in which the indirect reduction mediated by atomic H^* plays a leading role compared to the direct electron transfer from the cathode to NO_3^- [16]. Nevertheless, considering the extremely expensive price of Pd, the research significance of the Pd-based catalyst is obviously theoretical but not practical. Additionally, despite the fact that the indirect reduction mechanism of NO_3^- has been well explored in electrochemical noble metal-based process, the targeted strategies to develop some specific catalysts for the direct reduction of NO_3^- is sparsely reported.

The cost-effective cobalt oxide (Co_3O_4) is a typical p-type metal oxide, which exhibits a normal spinel structure with Co^{2+} ions in tetrahedral interstices and Co^{3+} ions in octahedral interstices. During the recent decades, Co_3O_4 has been demonstrated to own strong catalytic reduction activity and thus extensively used in electrochemical hydrogen evolution reaction [17] and reduction of CO_2 [18] and NO_x [19]. Recently, Su et al. [20] reported that the pure Co_3O_4 loaded onto the titanium substrate by thermal sintering could also electrocatalytically reduce NO_3^- in the water. However, the Co_3O_4 -mediated electrochemical mechanism of NO_3^- reduction has remained unclear. Moreover, it is known that the biologically toxic cobalt ion probably causes human carcinogen, and the discharge standard of cobalt ions in industrial wastewater is 1 mg L^{-1} based on GB/T 25467-2010 of China. Therefore, efforts should be made to improve the stability of the cobalt-based catalyst and prevent its leaching from the substrate and leaking into the water. To this end, we prepared a novel cathode, $\text{Co}_3\text{O}_4\text{-TiO}_2/\text{Ti}$, by combining sol-gel and calcination methods, which seems to be promising for remarkably facilitate the electrocatalytic reduction of NO_3^- . The effects of electrode preparation factors (calcination temperature and coating times) and operation parameters (pH, current density and chloride ions concentration) on NO_3^- reduction were also investigated. In addition, based on the characterization of the prepared catalysts using XRD, SEM, HRTEM, EDS elemental mapping and XPS, we tried to relate the results to the catalytic activity. Furthermore, electrochemical analyses, radical scavenging experiments and density functional theory calculations were utilized to inspect the possible NO_3^- reduction mechanisms.

2. Experimental section

2.1. Reagents and materials

Titanium (Ti) plate (99.99% purity, thickness 1.0 mm) and $\text{IrO}_2\text{-RuO}_2/\text{Ti}$ plate were purchased from Yunxuan Metallic Materials Co. Ltd. Potassium iodide (KI, > 99%), mercuric iodide red

(HgI_2 , > 99.5%), potassium sodium tartrate tetrahydrate ($\text{NaKC}_4\text{H}_4\text{O}_6 \cdot 4\text{H}_2\text{O}$, > 99%), sulfamic acid ($\text{NH}_2\text{SO}_3\text{H}$, > 99%), sulfanilamide ($\text{C}_6\text{H}_8\text{N}_2\text{O}_2\text{S}$, > 99%), titanium butoxide ($\text{C}_{16}\text{H}_{36}\text{O}_4\text{Ti}$), cobalt hexahydrate ($\text{Co}(\text{NO}_3)_2 \cdot 6\text{H}_2\text{O}$, > 99%), sodium chloride (NaCl , > 99.5%), sodium pyrophosphate ($\text{Na}_4\text{P}_2\text{O}_7$, > 99%), cobaltic oxide (Co_2O_3 , > 99%), sodium acetate ($\text{C}_2\text{H}_3\text{NaO}_2$, > 99%), ethanol (95%), hexadecyl trimethyl ammonium bromide ($\text{C}_{19}\text{H}_{42}\text{BrN}$, TBA, > 99%), polyvinyl pyrrolidone K30 ($(\text{C}_6\text{H}_9\text{NO})_n$, PVP), ammonium chloride (NH_4Cl , 99.8%), potassium nitrate (KNO_3 , > 99.5%), sodium nitrite (NaNO_2 , > 99%), H_2SO_4 (95%–98%), HCl (36%–38%), NaOH (> 96%) were provided by Sinopharm Chemical Reagent Co. Ltd., China. All the reagents were analytical grade and used without further purification. All working solutions were prepared using ultrapure water (18.2 M Ω cm resistivity). The experiments were done triplicate.

2.2. Preparation of the working cathode

The substrate of electrode was Ti plate with size of $2.5 \times 5.0 \text{ cm}$. The Ti plate was first polished with 300-mesh emery paper and then boiled in 20% sulfuric acid for 40 min. Next, the Ti plate was cleaned by ultrapure water, sonicated for 15 min, and dried for use. To synthesize the typical $\text{Co}_3\text{O}_4\text{-TiO}_2/\text{Ti}$ cathode, 0.5 mL titanium butoxide, 0.1 mL hydrochloric acid and 0.15 mL ultrapure water were dissolved in 8.5 mL ethyl alcohol. Then, 0.5 g PVP was added and stirred vigorously for 0.5 h. Subsequently, 2.69 g $\text{Co}(\text{NO}_3)_2 \cdot 6\text{H}_2\text{O}$ (1 M) was added and stirred to obtain a purplish red liquid. The prepared sol-gel was pasted to the both faces of the pretreated Ti plates using a brush. The painted Ti plate was dried at 100°C for 10 min. Then it was sintered at 500°C for 2 h in a muffle oven to remove all organic substances with the formation of the oxide. The above procedures were repeated 4 times and the electrode films were annealed for 6 h at 500°C in the last time. Other different kinds of cathodes were prepared with the same process with that for the $\text{Co}_3\text{O}_4\text{-TiO}_2/\text{Ti}$ (without PVP) cathode. Furthermore, the coating times (2, 4, 6 and 8) and the calcination temperatures (300°C , 400°C , 500°C , 600°C and 700°C) were adjusted to optimize the preparation factors.

2.3. Electrocatalytic reduction of NO_3^-

A DC potentiostat (GPS-3030D, Gwinstek, China) was utilized as the power supply for electrochemical experiments. The electrocatalytic NO_3^- reduction experiments were carried out in a 150 mL electrolytic cell at room temperature (25°C). If not specially mentioned, the volume of the working solution was 100 mL, NO_3^- concentration was 50 mg L^{-1} , and 0.1 M Na_2SO_4 was used as supporting electrolyte to maintain the conductivity of the solution. The solution pH was adjusted using concentrated NaOH and H_2SO_4 . The 12.5 cm^2 $\text{Co}_3\text{O}_4\text{-TiO}_2\text{-PVP}$ electrodes were used as cathode and 12.5 cm^2 $\text{IrO}_2\text{-RuO}_2/\text{Ti}$ electrodes were used as anode. The distance between the electrodes was 2 cm. The typical electrochemical experiment was conducted at current density of 10 mA cm^{-2} . All experiments were repeated at least twice.

2.4. Physicochemical characterizations and DFT calculation

The crystalline nature of the surface of $\text{Co}_3\text{O}_4\text{-TiO}_2/\text{Ti}$ cathode was examined by X-ray diffraction (XRD) measurement and the 2θ values acquired within the range of 10° to 80° using a Bruker D2 PHASER X-ray diffractometer that uses $\text{Cu K}\alpha$ radiation. The morphology of the cathode surface was depicted by a scanning electron microscopy (SEM, FEI QUANTA FEG250) and high-resolution transmission electron microscope (HRTEM, JEM-2100 F). The X-ray photoelectron spectroscopy (XPS) was obtained using a Thermo Fisher ESCALAB 250Xi system with Al $\text{K}\alpha$ as an X-ray source. C 1s peak at 284.8 eV from residual carbon was conducted to correct the binding energy of other elements. The details of DFT calculation were provided in the supplementary material.

2.5. Electrochemical characterizations

All electrochemical measurements were performed on an electrochemical station (PGSTAT 302 N, Metrohm). A standard three-electrode system was used in which the working electrode was a home made $\text{Co}_3\text{O}_4\text{-TiO}_2/\text{Ti}$ cathode, the counter electrode was a platinum plate, and the reference electrode was a saturated calomel electrode (SCE). The effective working area of the working and counter electrodes was 12.5 cm^2 . The electrolyte for linear sweep voltammetry (LSV) and cyclic voltammetry (CV) tests was composed of $0.1\text{ M Na}_2\text{SO}_4$ solution with or without $50\text{ mg L}^{-1}\text{ NO}_3^-$. CV tests were recorded between 0.0 V and -1.5 V/SCE at a scan rate of 20 mV s^{-1} . Electrochemical impedance spectroscopy (EIS) measurements were operated in $0.1\text{ M Na}_2\text{SO}_4$ solution using the frequency ranged from 10^5 to 10^{-2} Hz and the amplitude of the potential of 10 mV .

2.6. Chemical analyses

The concentrations of NO_3^- , NO_2^- and NH_4^+ were determined with a UV–vis spectrophotometer as it has been depicted in detail in the previous literature [21]. The residual NO_3^- ratio ($R_{\text{NO}_3^-}$), the generated NO_2^- ratio ($S_{\text{NO}_2^-}$), the generated NH_4^+ ratio, ($S_{\text{NH}_4^+}$), the total nitrogen (TN) removal efficiency, (R_{TN}) and N_2 selectivity (S_{N_2}), were calculated by the following equations:

$$R_{\text{NO}_3^-}(\%) = \frac{[\text{NO}_3^-]_0 - [\text{NO}_3^-]_t}{[\text{NO}_3^-]_0} \times 100 \quad (3)$$

$$S_{\text{NO}_2^-}(\%) = \frac{[\text{NO}_2^-]_t}{[\text{NO}_3^-]_0} \times 100 \quad (4)$$

$$S_{\text{NH}_4^+}(\%) = \frac{[\text{NH}_4^+]_t}{[\text{NO}_3^-]_0} \times 100 \quad (5)$$

$$R_{\text{TN}} = 1 - R_{\text{NO}_3^-} - S_{\text{NO}_2^-} - S_{\text{NH}_4^+} \quad (6)$$

$$S_{\text{N}_2}(\%) = \frac{R_{\text{TN}}}{1 - R_{\text{NO}_3^-}} \times 100 \quad (7)$$

where $[\text{NO}_3^-]_0$ is the initial concentration of NO_3^- and $[\text{NO}_3^-]_t$, $[\text{NO}_2^-]_t$, and $[\text{NH}_4^+]_t$ are the concentrations of NO_3^- , NO_2^- and NH_4^+ at time t .

3. Results and discussion

3.1. Catalytic NO_3^- reduction by different cathodes

The comparative NO_3^- reduction process efficiency at different cathodes was depicted in Fig. 1. As shown in Fig. 1(a), the NO_3^- removal efficiency of TiO_2/Ti cathode was only 45% at current density of 10 mA cm^{-2} after 120 min. However, as for $\text{Co}_3\text{O}_4\text{-TiO}_2/\text{Ti}$ (without PVP) cathode, NO_3^- removal efficiency suddenly became twice that of TiO_2/Ti cathode, reaching approximately 80%. Moreover, with the introduction of the dispersant PVP, the removal efficiency of NO_3^- was further increased to 89%. Although the addition of TiO_2 resulted in a slight decrease (nearly 6%) in the removal efficiency of NO_3^- compared to $\text{Co}_3\text{O}_4/\text{Ti}$ cathode, the release of Co ions into the aqueous solution was remarkably inhibited, probably due to the stabilization effect of TiO_2 (see Fig. 1(b)). In the case of $\text{Co}_3\text{O}_4/\text{Ti}$ cathode, the leaching of Co ions ($\text{Co}^{2+}/\text{Co}^{3+}$) reached 0.2 mg L^{-1} after 120 min, while Co ions were barely detected for both the $\text{Co}_3\text{O}_4\text{-TiO}_2/\text{Ti}$ and $\text{Co}_3\text{O}_4\text{-TiO}_2/\text{Ti}$ (without PVP) cathodes. Recently, many non-precious catalysts for NO_3^- reduction have been developed as the alternatives to conventional noble Pd catalyst. As shown in Table S1, the $\text{Co}_3\text{O}_4\text{-TiO}_2/\text{Ti}$ cathode exhibits significantly superior NO_3^- reduction activity over other non-precious electrodes.

As shown in Fig. 1(c), the profiles of ammonium (NH_4^+) formation as a function of electrolysis time have similar trends with those of NO_3^-

removal in the above reaction systems. The amount of NH_4^+ formed in the case of $\text{Co}_3\text{O}_4/\text{Ti}$ cathode was larger than those of $\text{Co}_3\text{O}_4\text{-TiO}_2/\text{Ti}$ and $\text{Co}_3\text{O}_4\text{-TiO}_2/\text{Ti}$ (without PVP) cathodes. In addition, among all the cathodes tested, the TiO_2/Ti produced the lowest amount of NH_4^+ , due to its inferior performance for NO_3^- reduction. During NO_3^- reduction process, the toxic intermediate NO_2^- was negligibly detected in the cases of $\text{Co}_3\text{O}_4\text{-TiO}_2/\text{Ti}$, $\text{Co}_3\text{O}_4\text{-TiO}_2/\text{Ti}$ (without PVP) and $\text{Co}_3\text{O}_4/\text{Ti}$ cathodes, while a significant amount (around 1%) of NO_3^- was transformed into NO_2^- when using TiO_2/Ti as the cathode. Although NO_3^- reduction efficiency of $\text{Co}_3\text{O}_4\text{-TiO}_2/\text{Ti}$ cathode was slightly lower than that of $\text{Co}_3\text{O}_4/\text{Ti}$ cathode, the TN removal efficiency and N_2 selectivity for the former were comparable to that of the latter as shown in Fig. S1. Besides, the TN removal efficiency and N_2 selectivity of $\text{Co}_3\text{O}_4\text{-TiO}_2/\text{Ti}$ (without PVP) and TiO_2/Ti cathodes were much lower than those of $\text{Co}_3\text{O}_4\text{-TiO}_2/\text{Ti}$ cathode.

Fig. 2 shows the XRD pattern of $\text{Co}_3\text{O}_4\text{-TiO}_2/\text{Ti}$ cathode calcinated at the temperature of 500°C . A comparison was performed between the obtained XRD data and standard patterns of various cobalt oxide and titanium oxide structures including cubic phase Co_3O_4 (PDF#42-1467), Ti (PDF#44-1294), anatase TiO_2 (PDF#21-1272), and rutile TiO_2 (PDF#21-1276). It is observed that all the detectable peaks agree well with standard cubic phase Co_3O_4 , anatase TiO_2 , and rutile TiO_2 . And the main characteristic peaks of Co_3O_4 are at $2\theta = 31.3^\circ$, 36.9° , 38.6° , 44.8° , 59.4° , 65.2° , 77.3° , which correspond to (220), (311), (222), (400), (511), (440), and (533) planes, respectively. This shows that the main components of the as-prepared cathode were the target catalyst Co_3O_4 and the dispersant carrier TiO_2 .

SEM images (Fig. 3) illustrate the morphology of as-prepared catalysts. Fig. 3(a)–(c) correspond to $\text{Co}_3\text{O}_4\text{-TiO}_2/\text{Ti}$, $\text{Co}_3\text{O}_4\text{-TiO}_2/\text{Ti}$ (without PVP), and $\text{Co}_3\text{O}_4/\text{Ti}$ cathodes, respectively. It can be clearly seen that Co_3O_4 particles on $\text{Co}_3\text{O}_4\text{-TiO}_2/\text{Ti}$ cathode were small and uniform, whereas that on $\text{Co}_3\text{O}_4\text{-TiO}_2/\text{Ti}$ (without PVP) and $\text{Co}_3\text{O}_4/\text{Ti}$ cathodes were apparently agglomerated and represented in the forms of disordered nanotubes and irregular aggregates, respectively, showing the successful role of PVP as surface dispersant by mixing PVP and metal-salt precursor solution [22]. Fig. 3(d)–(h) provide the EDS maps of Co and Ti elements at the above three cathodes. Obviously, the presence of PVP could effectively improve the uniformity of Co and Ti distribution on the surface of $\text{Co}_3\text{O}_4\text{-TiO}_2/\text{Ti}$ cathode, which was therefore better than that of $\text{Co}_3\text{O}_4\text{-TiO}_2/\text{Ti}$ (without PVP) cathode. As for $\text{Co}_3\text{O}_4/\text{Ti}$ cathode, the aggregation of Co element was more pronounced in comparison with the other two cathodes, indicating the worst distribution of Co_3O_4 on $\text{Co}_3\text{O}_4/\text{Ti}$ cathode. The electrocatalytic property could be improved by using PVP as surface stabilizer and growth modifier since it could effectively alleviate the agglomeration of the catalysts and enhance the relative population of stable clusters during the synthesis of nanoparticles (NPs), thereby more active sites are exposed at the cathode surface. [23,24] Therefore, it can be concluded that both the TiO_2 and the PVP dispersant could evidently promote the distribution and stability of Co_3O_4 on the Ti plate, which will expose more active sites and inhibit the leaching of catalyst from the electrode surface. This may explain the superior catalytic performance and stability of $\text{Co}_3\text{O}_4\text{-TiO}_2/\text{Ti}$ cathode over $\text{Co}_3\text{O}_4\text{-TiO}_2/\text{Ti}$ (without PVP) and $\text{Co}_3\text{O}_4/\text{Ti}$ cathodes as shown in the Fig. 1. HRTEM images of $\text{Co}_3\text{O}_4\text{-TiO}_2/\text{Ti}$ in Fig. 4(a) presents dark Co_3O_4 species with a 10–50 nm diameter. The primarily exposed crystal planes of as-synthesized Co_3O_4 are (311) with the lattice spacing (d) of 0.244 nm (Fig. 4(b)), which is consistent with the XRD patterns.

3.2. Preparation parameters

3.2.1. Effect of coating times

The Co ions concentration of 0, 0.5, 1.0, and 2.0 M with 4 coating times was investigated. The NO_3^- concentration decay kinetics and LSV curves (Fig. S2) demonstrate that 1.0 M was compatible. In this section, the studied number of coating times was 2, 4, 6, and 8 with Co

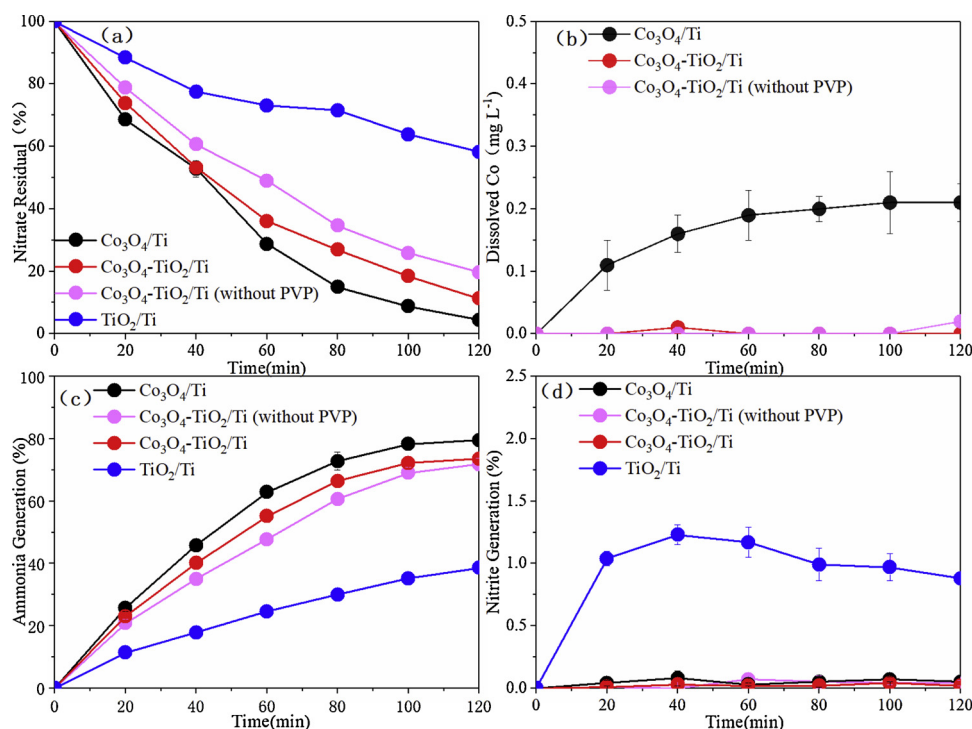


Fig. 1. NO_3^- concentration decay kinetics (a), and evolution of concentration of Co (b), NH_4^+ (c) and NO_2^- (d) during electrolysis time. Experimental conditions: $[\text{NO}_3^-]_0 = 50 \text{ mg L}^{-1}$, $\text{pH} = 7.0$, current density = 10 mA cm^{-2} .

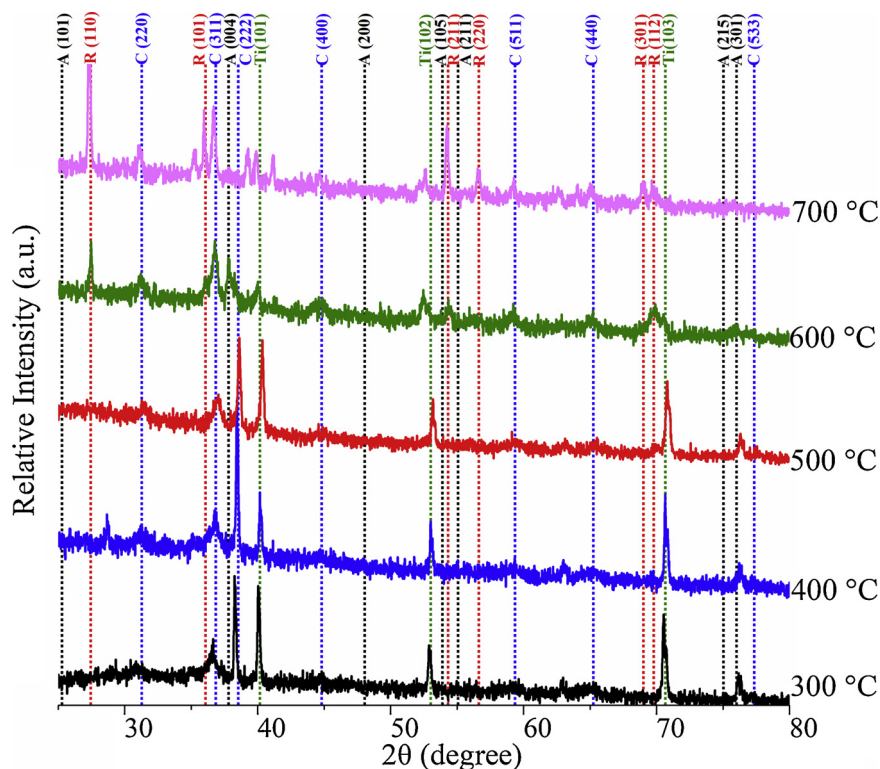


Fig. 2. XRD patterns of $\text{Co}_3\text{O}_4\text{-TiO}_2/\text{Ti}$ cathodes calcined at 300 °C, 400 °C, 500 °C, 600 °C and 700 °C. The locations of the characteristic peaks for Co_3O_4 (C), Ti substrate (Ti), anatase (A), and rutile (R) are represented by the vertical dashed lines.

ions concentration of 1.0 M, which was represented as 2- $\text{Co}_3\text{O}_4\text{-TiO}_2/\text{Ti}$, 4- $\text{Co}_3\text{O}_4\text{-TiO}_2/\text{Ti}$, 6- $\text{Co}_3\text{O}_4\text{-TiO}_2/\text{Ti}$ and 8- $\text{Co}_3\text{O}_4\text{-TiO}_2/\text{Ti}$ cathodes, respectively. Although, as shown in Fig. S3, the coating times negligibly affected the morphology of the electrode surface, too many or too few coating times were not conducive to NO_3^- reduction. The NO_3^-

removal efficiencies for 2- $\text{Co}_3\text{O}_4\text{-TiO}_2/\text{Ti}$, 4- $\text{Co}_3\text{O}_4\text{-TiO}_2/\text{Ti}$, 6- $\text{Co}_3\text{O}_4\text{-TiO}_2/\text{Ti}$ and 8- $\text{Co}_3\text{O}_4\text{-TiO}_2/\text{Ti}$ cathodes were 80%, 89%, 64% and 61%, respectively, within 120 min. Thus, the optimum number of coating times was 4. As illustrated in Fig. 5(b), 4- $\text{Co}_3\text{O}_4\text{-TiO}_2/\text{Ti}$ cathode has the largest response current intensity. And the trend of response current

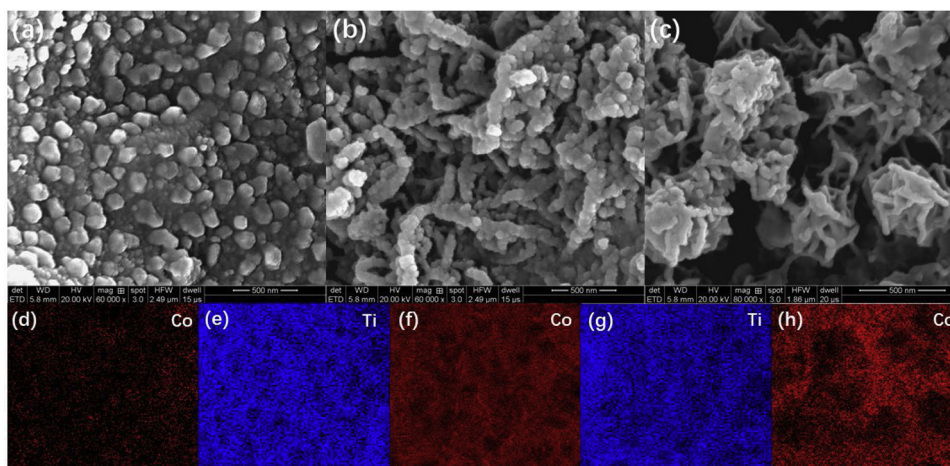


Fig. 3. SEM images of $\text{Co}_3\text{O}_4\text{-TiO}_2/\text{Ti}$ (a), $\text{Co}_3\text{O}_4\text{-TiO}_2/\text{Ti}$ (without PVP) (b) and $\text{Co}_3\text{O}_4/\text{Ti}$ (c) cathodes. Elemental mapping of $\text{Co}_3\text{O}_4\text{-TiO}_2/\text{Ti}$ (d,e), $\text{Co}_3\text{O}_4\text{-TiO}_2/\text{Ti}$ (without PVP) (f,g) $\text{Co}_3\text{O}_4/\text{Ti}$ (h) cathodes. Elemental mapping: (d–h) correspond to Co, Ti, Co, Ti and Co maps, respectively.

intensity at the same voltage was consistent with the NO_3^- reduction trend of Fig. 5(a). The above experimental and LSV results can be explained by the fact that when the number of coating times was below 4, insufficient Co loadings may not afford enough active sites for NO_3^- reduction. In contrast, when the number of coating times was more than 4, the catalyst coating on the Ti plate was thick, which probably deteriorated the electron transfer, and the increased potential would exacerbate the occurrence of hydrogen evolution side reactions, therefore led to a decrease in NO_3^- reduction efficiency.

3.2.2. Effect of calcination temperature

In this section, the effect of calcination temperatures on the performance of $\text{Co}_3\text{O}_4\text{-TiO}_2/\text{Ti}$ cathode was investigated. The as-prepared cathodes sintered at 300 °C, 400 °C, 500 °C, 600 °C and 700 °C were marked as 300- $\text{Co}_3\text{O}_4\text{-TiO}_2/\text{Ti}$, 400- $\text{Co}_3\text{O}_4\text{-TiO}_2/\text{Ti}$, 500- $\text{Co}_3\text{O}_4\text{-TiO}_2/\text{Ti}$, 600- $\text{Co}_3\text{O}_4\text{-TiO}_2/\text{Ti}$ and 700- $\text{Co}_3\text{O}_4\text{-TiO}_2/\text{Ti}$, respectively. Fig. 6(a) shows that there were significant differences in NO_3^- reduction efficiency between the cathodes sintered at different temperatures. The optimum NO_3^- removal efficiency was observed for the cathode calcination in the temperature range of 300–500 °C, e.g., approximately 89% for 500- $\text{Co}_3\text{O}_4\text{-TiO}_2/\text{Ti}$ cathode. A moderate NO_3^- removal efficiency was obtained for 600- $\text{Co}_3\text{O}_4\text{-TiO}_2/\text{Ti}$ cathode (67%) while the 700- $\text{Co}_3\text{O}_4\text{-TiO}_2/\text{Ti}$ cathode had the marginal NO_3^- removal efficiency, approximately 34%. The variation trend of response current intensity observed from the LSV measurements (Fig. 6(b)) was in good accordance with that of the cathodes for NO_3^- removal, which confirmed the best performance of the 500- $\text{Co}_3\text{O}_4\text{-TiO}_2\text{-PVP}$ cathode.

As shown in Fig. 2, the main characteristic peaks of Co_3O_4 in XRD spectra for $\text{Co}_3\text{O}_4\text{-TiO}_2/\text{Ti}$ cathode became narrower and sharper as the calcination temperature increased in the range of 300–700 °C. According to the previous studies, complete conversion of Co_3O_4 can be

achieved in the sol-gel and calcination process when the temperature exceeds 270 °C [20]. Better crystallinity structure of Co_3O_4 could be obtained at higher calcination temperatures. Nevertheless, Ti plate has some problems when being sintered at relatively high temperature. Specially, as demonstrated in the previous literature [20], the conductivity of Ti plate was greatly reduced when the calcination temperature reached 600 °C. Besides, the phase structure, composition, and crystallinity of TiO_2 are of great influence on its electrocatalytic activity and electrochemical properties [25]. Therefore, XRD was also used to analyze the changes of TiO_2 phase on the cathodes sintered at various temperatures. It can be seen from the XRD patterns presented in Fig. 2 that the calcination temperature significantly impacted the crystallization and phase structures of surface catalysts on $\text{Co}_3\text{O}_4\text{-TiO}_2/\text{Ti}$ cathode. For $\text{Co}_3\text{O}_4\text{-TiO}_2/\text{Ti}$ cathodes sintered at the temperature of 300–500 °C, except the diffraction peaks of Ti substrate and Co_3O_4 , two broad peaks at $2\theta = 53.9^\circ$ and 76.0° can be attributed to the (105) and (301) plane diffraction, respectively, of anatase TiO_2 . However, as for 600- $\text{Co}_3\text{O}_4\text{-TiO}_2/\text{Ti}$ cathode, small peaks at $2\theta = 27.4^\circ$, 36.1° , 54.3° , 56.6° , 69.0° , and 69.8° correspond to (110), (101), (211), (220), (301), and (112) plane diffraction, respectively, of rutile. Notably, the intensity of rutile diffraction peaks of $\text{Co}_3\text{O}_4\text{-TiO}_2/\text{Ti}$ cathode increases sharply at the calcination temperature of 700 °C. This suggests the occurrence of phase transformation of anatase to rutile when elevating the calcination temperature from 300 to 600 °C, which was even more pronounced for 700 °C. Furthermore, with the calcination temperature increase to 600 °C and 700 °C, the crystal turned to aggregation, which was probably responsible for the decrease of NO_3^- reduction efficiency (Fig. S4). Based on these results, it can be concluded that the phase transformation of TiO_2 began to take place at the calcination temperature above 500 °C. When calcination temperature reaches 600 °C, the rutile phase even became the prevalent phase of the composite. This

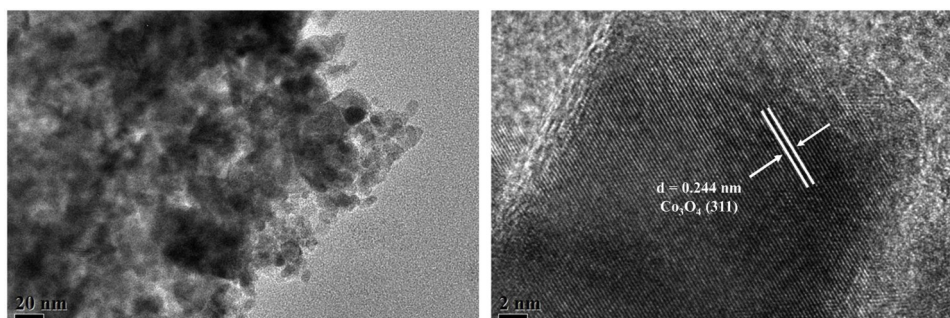


Fig. 4. HRTEM images of $\text{Co}_3\text{O}_4\text{-TiO}_2/\text{Ti}$.

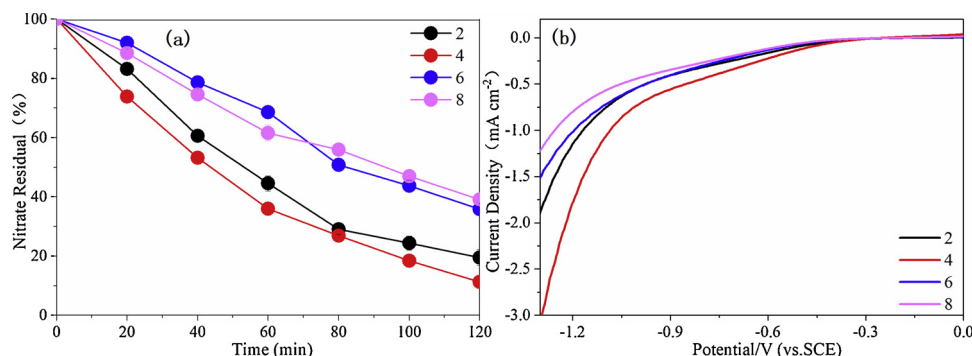


Fig. 5. NO_3^- concentration decay kinetics (a) and LSV curves (b) for different coating times. Experimental conditions: (a) $[\text{NO}_3^-]_0 = 50 \text{ mg L}^{-1}$, pH = 7.0, current density = 10 mA cm^{-2} , (b) $0.1 \text{ M SO}_4^{2-} + 50 \text{ mg L}^{-1} \text{ NO}_3^-$ solution, scan rate: 100 mV s^{-1} .

was consistent with the results in the previous literature papers [26].

Based on the EIS measurements, the Nyquist plots of various $\text{Co}_3\text{O}_4\text{-TiO}_2/\text{Ti}$ cathodes sintered at various temperatures are provided in Fig. 6(c). The radius of semicircle was related with the charge transfer resistance and the sample with smaller arc radius indicates faster interfacial electron transfer [27]. The calcination temperature exerts a significant effect on the electrochemical properties of the electrodes. In this study, when the calcination temperature was increased from 300 to 500 °C, the radius of the arc did not appear, indicating that the charge transfer resistance was small. However, when the calcination temperature rose to 600 °C, the arc radius appeared, suggesting the fact that increasing calcination temperature caused an increase in impedance for $\text{Co}_3\text{O}_4\text{-TiO}_2/\text{Ti}$ cathode. And the charge transfer resistance of $\text{Co}_3\text{O}_4\text{-TiO}_2/\text{Ti}$ cathode obtained at the calcination temperature of 700 °C was larger than that of 600 °C. The change of EIS results indicates that the phase transformation of anatase to rutile with elevating calcination temperature could inhibit the charge transfer within the cathode, which adverse to NO_3^- reduction [28]. This can be ascribed to the higher electric resistance of rutile than that of anatase [28].

Therefore, the relatively low NO_3^- reduction efficiencies for 600- $\text{Co}_3\text{O}_4\text{-TiO}_2/\text{Ti}$ and 700- $\text{Co}_3\text{O}_4\text{-TiO}_2/\text{Ti}$ cathodes could be explained by the increase in the charge transfer resistance of $\text{Co}_3\text{O}_4\text{-TiO}_2/\text{Ti}$ cathode prepared at a high calcination temperature. Consequently, appreciable $\text{Co}_3\text{O}_4\text{-TiO}_2/\text{Ti}$ cathodes could be obtained at the calcination temperature of 300–500 °C, in which cobalt precursor could be completely transformed to Co_3O_4 and the relatively low charge transfer resistance could be also ensured.

3.3. Effect of electrochemical reaction parameters

3.3.1. Effect of solution pH and current density

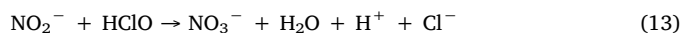
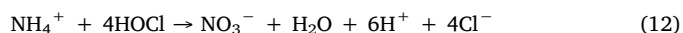
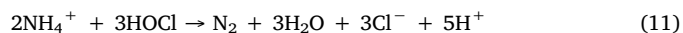
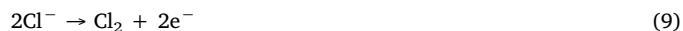
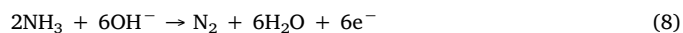
As illustrated in Fig. 7, the effect of solution pH (3.0–9.0) on NO_3^- reduction was evaluated in this section. Fig. 7(a) and (b) show the reduction curves of NO_3^- over time and the final solution pH for different initial pH values. Contrarily to the previous studies [29], Fig. 7(a) shows that different pH conditions did not play significant role on NO_3^- reduction efficiency over the electrolysis time. This indicates that $\text{Co}_3\text{O}_4\text{-TiO}_2/\text{Ti}$ cathode prepared in this study has a wide working pH range and can be potentially used to treat the NO_3^- containing wastewaters in a relatively large pH range. Besides, Fig. 7(b) shows that, regardless of the initial pH, the pH value was significantly increased after 120 min reaction. For example, after 2 h of nitrate reduction, the solution pH increased from 3.0, 5.0, 7.0 and 9.0 to 9.0, 10.6, 10.9 and 11.0, respectively. The explanation for this pH variation will be discussed in the following Section 3.4.

On the other hand, the reduction efficiency of NO_3^- was significantly enhanced with the increase of current density from 2.5 to 10 mA cm^{-2} (Fig. 8(a)). However, when the current density was increased from 10 to 25 mA cm^{-2} , the removal efficiency of NO_3^- was not

greatly improved. Fig. S5 shows that the reduction of $50 \text{ mg L}^{-1} \text{ NO}_3^-$ followed a zero-order kinetic trend at the current density of 2.5 and 5 mA cm^{-2} with the rate constant increased from 0.190 ($R^2 = 0.99$) to 0.440 ($R^2 = 0.98$) min^{-1} (indicating a charge controlled kinetic stage) while a first-order kinetic trend was observed at the current densities of 10 and 25 mA cm^{-2} (indicating a mass controlled kinetic stage) with the rate constant of 0.018 ($R^2 = 0.99$) and 0.027 ($R^2 = 0.99$) min^{-1} , respectively. As the current density was increased from 10 to 25 mA cm^{-2} , more energy was used to generate hydrogen bubble, so that the increase in the NO_3^- removal efficiency was not significant as expected. There is a good correspondence between the amount of NH_4^+ produced and the amount of NO_3^- reduced as shown on Fig. 8(b). Low current density leads to lower energy consumption, but in actual use, it is necessary to seek the balance between the energy saving and the NO_3^- treatment requirements to gain the highly appreciable treatment performance.

3.3.2. Effect of chlorine concentration

As can be seen in Fig. S1, the main product of the electrocatalytic reduction of NO_3^- was NH_4^+ , which is also a contaminant that needed to be removed. The removal of NH_3 is primarily takes place through direct oxidation on the anode surface and indirect oxidation mediated by active chlorine in the solution bulk. In the direct oxidation process, the NH_3 is first adsorbed on the surface of the anode and subsequently oxidized to N_2 , as shown in Eq. (8) [30]. However, NH_4^+ cannot be oxidized directly at the anode. Hence it is necessary to adjust the solution pH to reach the pK_a of the $\text{NH}_4^+/\text{NH}_3$ acid-base pair (i.e., pH > 9.25). [32] In addition to the direct oxidation of NH_3 on the anode, the generated active chlorine species (Eqs. (9) and (10)) at the anode could also be involved in the oxidative transformation of NH_4^+ to nitrogen gas (Eq. (11)) or NO_3^- (Eq. (12)) as well as the oxidation of NO_2^- to NO_3^- (Eq. (13)) in the homogeneous solution, so-called indirect (or mediated) oxidation [30]. Furthermore, HOCl reacts also on NH_3 to form chloramines (Eqs. (14)–(16)). Compared with direct ammonia oxidation, the chlorine-mediated ammonia oxidation is much more efficient and feasible due to the abundant presence of chloride ion in wastewaters.



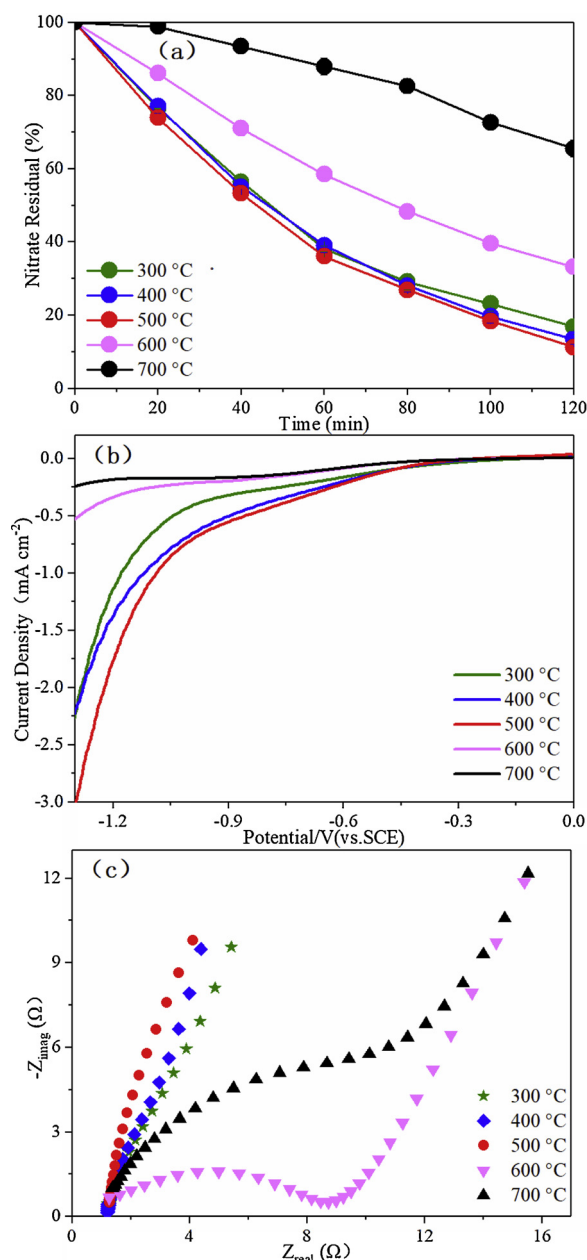


Fig. 6. NO_3^- concentration decay kinetics at different calcination temperature (a) under experimental conditions: $[\text{NO}_3^-]_0 = 50 \text{ mg L}^{-1}$, $\text{pH} = 7.0$, current density = 10 mA cm^{-2} , LSV curves at different calcination temperature (b) in $0.1 \text{ M SO}_4^{2-} + 50 \text{ mg L}^{-1} \text{ NO}_3^-$ solution at a scan rate of 100 mV s^{-1} and (c) EIS Nyquist plots of the cathodes at different calcination temperature by applying an impedance amplitude of 10 mV with the frequency range from 10^5 to 10^{-2} Hz .



Chloride ions are widely presented in drinking water and industrial water. For instance, the concentration of chloride ions in the bulk drug manufacturing industrial wastewater and zinc refinery wastewater reached 3119 and $10,000 \text{ mg L}^{-1}$, respectively [35]. Considering the role of chloride ions in oxidation of NH_4^+ , various concentrations of chloride ions were added to the solution in order to study its effect. As shown in Fig. 9(a), the NO_3^- removal efficiency was almost unaffected by the presence of chloride ions. But, as the concentration of chloride ions increased from 0 to 2000 mg L^{-1} , the formation of NH_4^+ progressively decreased (Fig. 9(b)). For instance, when the concentration of chloride ions increased to 2000 mg L^{-1} , the generated NH_4^+ ions ratio

initially slightly increased to 7% within 40 min but then gradually decreased to approximately 0 after 100 min reaction time. Besides, it appears from Fig. 9(c) that the formation of NO_2^- could be deteriorated with increasing chloride ions concentration from 0 to 2000 mg L^{-1} , with the highest NO_2^- generation of 0.47% . It can also be seen from Fig. S6 that the TN removal efficiency and N_2 selectivity of $\text{Co}_3\text{O}_4\text{-TiO}_2/\text{Ti}$ cathode increased with the increase of chloride ions concentration. When the chloride ions concentration reached 2000 mg L^{-1} , the TN removal efficiency and N_2 selectivity reached 82% and 100% , respectively.

NH_4^+ formation curves plotted in Fig. 9(d) clearly show that its amount formed at $\text{Co}_3\text{O}_4/\text{Ti}$ cathode (49%) was about twice of that formed at $\text{Co}_3\text{O}_4\text{-TiO}_2/\text{Ti}$ cathode (24%) after 120 min reaction at the same chloride ions concentration of 1000 mg L^{-1} . Fig. S6 shows that the TN removal efficiency and N_2 selectivity for $\text{Co}_3\text{O}_4\text{-TiO}_2/\text{Ti}$ cathode were 60% and 71% , respectively, while the corresponding values for $\text{Co}_3\text{O}_4/\text{Ti}$ cathode were 42% and 46% , respectively. The difference in NT removal efficiency between $\text{Co}_3\text{O}_4\text{-TiO}_2/\text{Ti}$ and $\text{Co}_3\text{O}_4/\text{Ti}$ cathodes in the presence of chloride ions was much larger than in the chloride-free cases as observed in Fig. S1. The indirect oxidation mechanism of NH_4^+ was similar to the intensively studied breakpoint chlorination [31]. First, the NH_4^+ reacts with the active chlorine (HOCl or OCl depending to the solution the pH) to produce intermediate products such as monochloramine, dichloramine and tri-chloramine, and were finally oxidized to N_2 [32]. It is worth noting that the oxidation process of the NH_4^+ began to occur only when active chlorine/ammonia mole ratio reaches 1.5 [33]. Specially, Ding et al. [34] found that higher active chlorine/ammonia mole ratio (> 5) brought about 100% removal of NH_4^+ , while less efficient removal efficiencies (nearly 50%) were achieved with lower mole ratio (< 2). Thus, it can be inferred that electrochemical ammonia oxidation in these reaction systems was closely related with the active chlorine/ammonia mole ratio. As demonstrated in Fig. 1, the efficiency of NO_3^- reduction to NH_4^+ with $\text{Co}_3\text{O}_4/\text{Ti}$ cathode was higher than that with $\text{Co}_3\text{O}_4\text{-TiO}_2/\text{Ti}$ cathode. This would result in less mole ratio of active chlorine/ammonia in the former case compared with that in the latter case. Therefore, as shown in Fig. 9(d), the indirect oxidation of ammonia was more favorable for the $\text{Co}_3\text{O}_4\text{-TiO}_2/\text{Ti}$ cathode mediated electrochemical system.

3.4. The NO_3^- removal mechanism

3.4.1. Direct reduction

Electrochemical reduction of NO_3^- is a complex process involving a range of intermediates and broad valence changes (from $+5$ to -3). The process mainly includes direct reduction and indirect reduction. Direct reduction is mainly achieved by electrons and H^+ , and indirect reduction is mainly caused by atomic H^* [35]. This mechanism was verified in the present electrochemical reaction system by CV tests as depicted in Fig. 10(a). When $50 \text{ mg L}^{-1} \text{ NO}_3^-$ was added to the reaction solution, the peak current density of -2.4 and -4.0 mA cm^{-2} appeared at the potential of -0.9 and -1.2 V/SCE , respectively, at TiO_2/Ti cathode. These reduction peaks can be attributed to the electron transfer from the cathode to NO_3^- because no peak was observed in the absence of NO_3^- . Thus, it is rational that approximately 45% NO_3^- was reduced at TiO_2/Ti cathode (Fig. 1(a)). According to the previous studies [36], these two reduction peaks correspond to the reduction of NO_3^- to NO_2^- and the formation of NH_4^+ , respectively. Furthermore, single reduction peak does not mean single electron transfer [37]. In contrast, the peaks were completely disappeared in the case of $\text{Co}_3\text{O}_4\text{-TiO}_2/\text{Ti}$ cathode, regardless of the presence or absence of NO_3^- . Notably, the experimental results presented in Fig. 1 show that the NO_3^- reduction efficiency was greatly increased in the presence of Co_3O_4 . Therefore, the disappearance of the reduction peak was not ascribed to the poor catalytic activity of the Co_3O_4 toward the electrocatalytic reduction of NO_3^- . This peculiar phenomenon just became a breakthrough point to understand the mechanism of the NO_3^- electrocatalytic reduction by

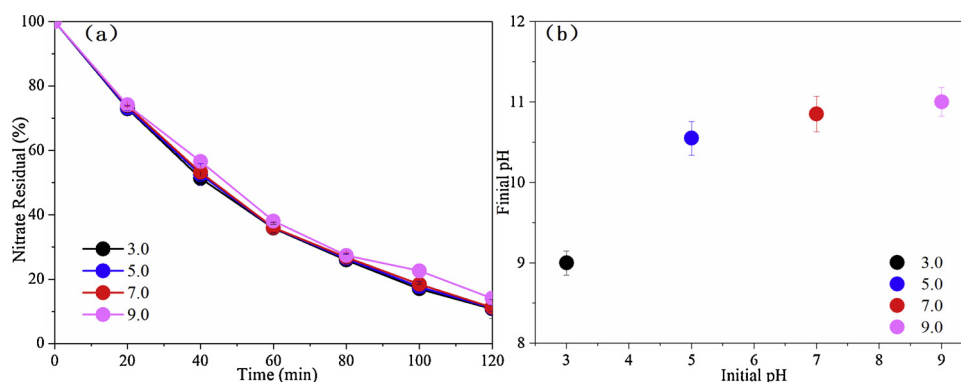


Fig. 7. NO_3^- concentration decay kinetics at different pH (a) and Final solution pH for various initial pH after 120 min reaction (b). Experimental conditions: $[\text{NO}_3^-]_0 = 50 \text{ mg L}^{-1}$, current density = 10 mA cm^{-2} .

Co_3O_4 . It is known that two processes, i.e., heterogeneous charge transfer and diffusional mass transport, mainly determine the shape of the CV curve [38]. The CV curve can reflect the heterogeneous charge transfer from the electrode to electroactive species. However, it fails to reflect the charge transfer and valence change inside the electrode. Co_3O_4 contains Co^{2+} ions in tetrahedral interstices and Co^{3+} ions in octahedral interstices. Thus, it can be inferred that NO_3^- probably did not directly receive electrons from the cathode via the circuit, but from the "electron porter" of the structural Co^{2+} ions. This proposition can be validated by the density functional theory (DFT) calculation results, which can be seen in Fig. 11. Co_3O_4 (222) was selected considering XRD detection and NO_3^- reduction experiments. The DFT calculation results show that the O atom in NO_3^- and the Co atom on the surface of Co_3O_4 (222) are thermodynamically favorably bonded with the required energy of -9.04 eV . Besides, the differential charge density distribution indicates that electrons can transfer from the Co atoms on the surface of Co_3O_4 (222) to NO_3^- . Differential charge density analysis further showed that the O atoms in NO_3^- obtained 0.41, 0.65, and 0.57 electrons, respectively, and the N atoms lost 0.82 electrons, and a total of 0.81 electrons were transferred from the Co atom to NO_3^- .

In order to further confirm this, the electrochemical reduction of NO_3^- at $\text{Co}_3\text{O}_4\text{-TiO}_2/\text{Ti}$ cathode was investigated at different cathode potentials, and the experimental results are shown in Fig. 10(b). Nearly no NO_3^- was removed at the applied potential of -0.5 and -0.7 V/SCE within 120 min. The NO_3^- removal efficiency of 36% and 40% were attained at -1.0 and -1.2 V/SCE , respectively. Besides, NO_3^- removal efficiency finally raised to 98% after 120 min electrolysis when the applied potential was further decreased to -1.3 V/SCE . However, the NO_3^- reduction efficiency was decreased to approximately 94% when further decreasing the cathode potential to -1.5 V/SCE . This can be attributed to the enhancement of hydrogen evolution reaction at this potential and the hindrance of hydrogen bubbles to the electron transfer at the cathode surface [39]. The strong dependence of NO_3^-

reduction on the cathode potential corresponding to reduction peaks of CV curve is in agreement with the literature [40]. This confirms the above conjecture that electrons were transferred from the power source to the cathode surface through a circuit, in which Co^{3+} was reduced to Co^{2+} via accepting an electron. Then nitrogen-containing contaminants, such as NO_3^- , receive the electrons from the structural Co^{2+} ions. This particular reaction process cannot be directly detected by CV test, explaining the disappearance of the reduction peak in Fig. 10(a) and the strong voltage-dependent phenomenon in Fig. 10(b).

In the above process, the ratio $\text{Co}^{2+}/\text{Co}^{3+}$ would definitely change. To further confirm this statement, XPS analysis was used. The XPS wide-survey scan of $\text{Co}(2p)$ is illustrated in Fig. 10(c). The peaks at 780 and 795 eV (binding energy) should be assigned to $\text{Co}(2p_{3/2})$ and $\text{Co}(2p_{1/2})$, respectively [41]. The $\text{Co}(2p_{3/2})/\text{Co}(2p_{1/2})$ ratio value of almost 2:1 was consistent with the previous literature report [42]. The peaks of Co^{2+} were located at 781.5 and 796.6 eV, while the peaks at 780 and 794.8 eV should be assigned to Co^{3+} [43,44]. Besides, the peaks at 786.8 and 804 eV were attributed to the shake-up satellite peaks of Co^{2+} [45]. Moreover, the $\text{Co}^{2+}/\text{Co}^{3+}$ ratios of the pristine and used $\text{Co}_3\text{O}_4\text{-TiO}_2/\text{Ti}$ cathodes were calculated as 1.49 and 0.42, respectively, which indicated the transformation of Co^{2+} to Co^{3+} during the electrochemical NO_3^- reduction process. This confirms the electrochemical redox cycle $\text{Co}^{2+}-\text{Co}^{3+}-\text{Co}^{2+}$ and the electron transfer from Co^{2+} to NO_3^- during the electrocatalytic NO_3^- reduction process.

3.4.2. Indirect reduction

In the indirect pathway, electrons from the cathode could produce surface-adsorbed atomic H^* via the reduction of protons, which is known as Volmer process [15]. Here, we employed CV technique to qualitatively detect the formed H^* during the electrochemical reaction process, which has been well introduced by Jiang et al. [46] and Liu et al. [47]. First, the cathode was repeatedly scanned for activation in a

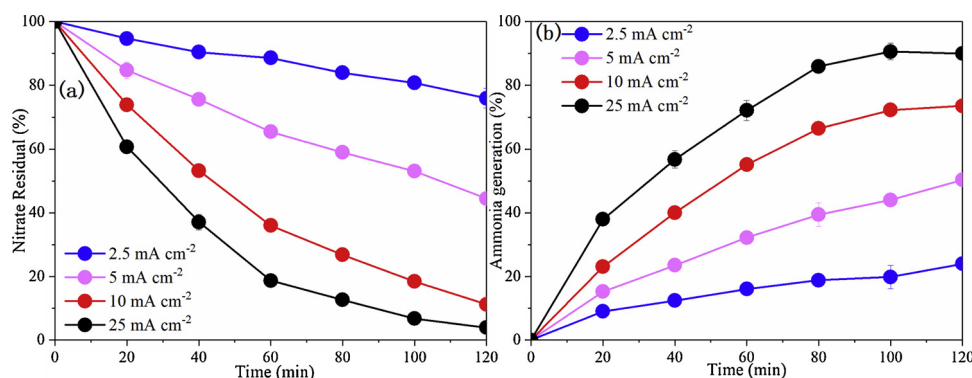


Fig. 8. NO_3^- concentration decay kinetics (a) and NH_4^+ generation (b) at different current density. Experimental conditions: $[\text{NO}_3^-]_0 = 50 \text{ mg L}^{-1}$, pH = 7.0.

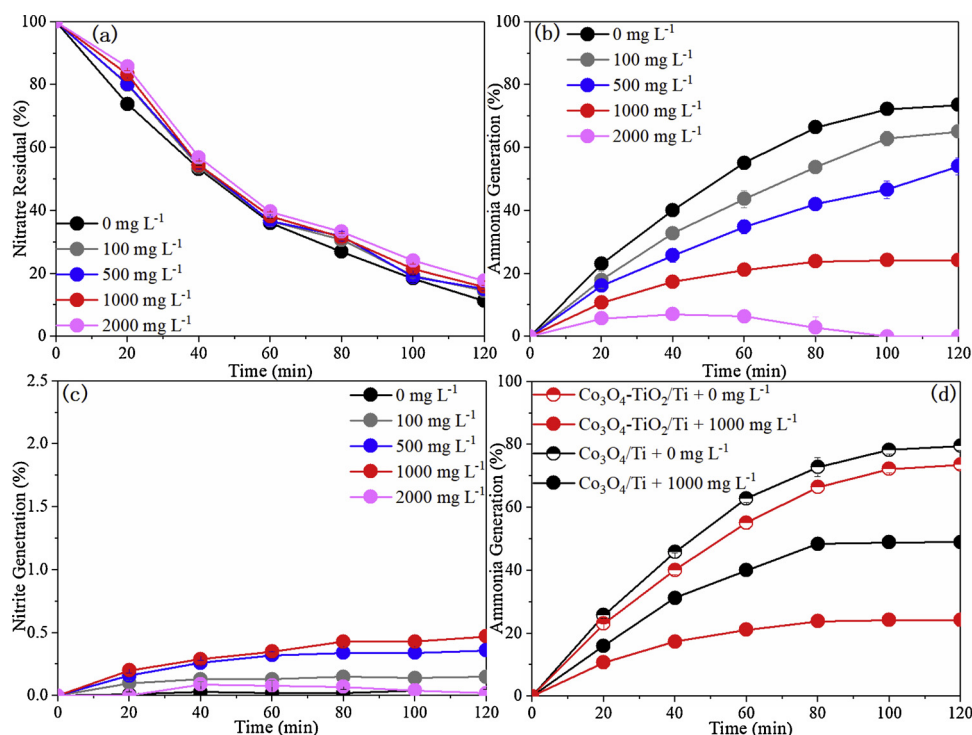


Fig. 9. Effect of Cl^- concentration on NO_3^- decay kinetics (a), NH_4^+ generation (b), NO_2^- generation (c) with $\text{Co}_3\text{O}_4\text{-TiO}_2/\text{Ti}$ cathode, and NH_4^+ generation with $\text{Co}_3\text{O}_4\text{-TiO}_2/\text{Ti}$ and $\text{Co}_3\text{O}_4/\text{Ti}$ cathodes (d). Experimental conditions: $[\text{NO}_3^-]_0 = 50 \text{ mg L}^{-1}$, $\text{pH} = 7.0$, current density = 10 mA cm^{-2} .

potential range of -0.20 to 0.90 V/SCE in $0.1 \text{ M Na}_2\text{SO}_4$ electrolyte at sweep rate of 100 mV s^{-1} . Electrochemical analysis did not start until a stable CV curve was obtained [46]. As shown in Fig. 10(d), the starting potential was set from -1.20 to -1.35 V/SCE and the termination potential was 0.45 V/SCE . As reported in the previous study involving C–Pd cathode for nitrate reduction [46]; the lower the starting potential, the stronger the corresponding oxidation peak. And the oxidation peaks of molecular hydrogen and atomic H^* were located at -0.80 to -0.60 V/SCE and -0.10 to -0.00 V/SCE , respectively. Fig. 10(d)

shows that at different initial potentials, reduction peaks were observed at the potentials from -0.6 to -0.1 V/SCE , corresponding to the oxidation of molecular H_2 and H^* , respectively. After adding 10 mM TBA , the intensity of the oxidation peak corresponding to atomic H^* immediately weakened. This markedly suppressed the availability of the formed H^* for the NO_3^- reduction.

Fig. 10(e) and (f) show LSV curves and NO_3^- reduction results, respectively, after the addition of 10 mM TBA . As illustrated in Fig. 10(e), the current intensity was significantly enhanced after the

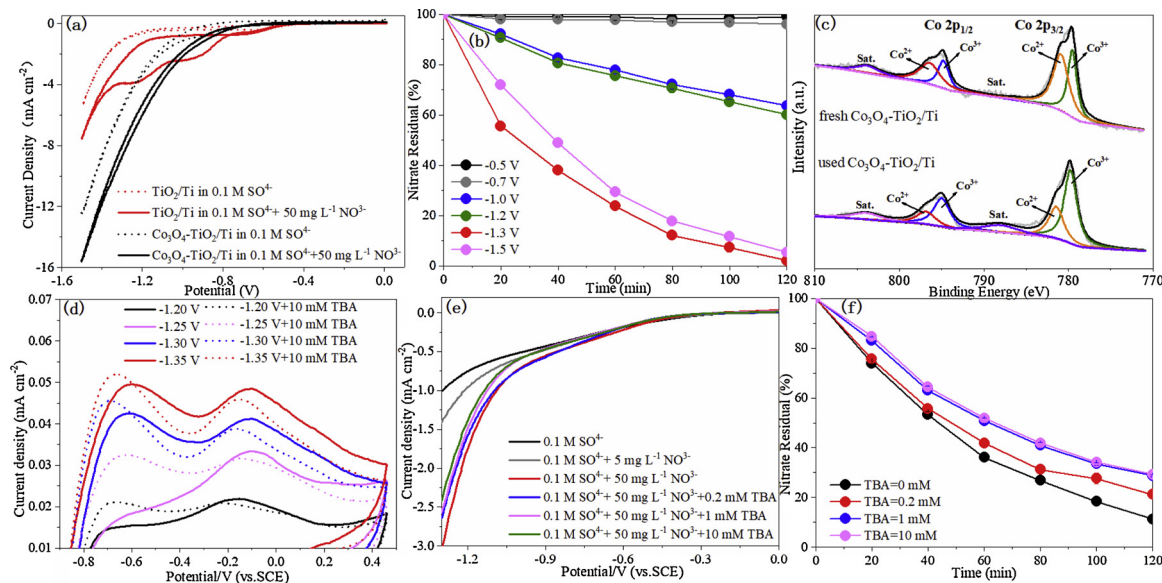


Fig. 10. Cyclic voltammograms of NO_3^- reduction (a) at TiO_2/Ti and $\text{Co}_3\text{O}_4\text{-TiO}_2/\text{Ti}$ cathodes (scan rate: 20 mV s^{-1}); Effect of cathode potential on NO_3^- concentration decay kinetics (b) at $\text{Co}_3\text{O}_4\text{-TiO}_2/\text{Ti}$ cathode (Experimental conditions: $[\text{NO}_3^-]_0 = 50 \text{ mg L}^{-1}$, $\text{pH} = 7.0$, current density = 10 mA cm^{-2}); XPS spectra of Co 2p for fresh and used $\text{Co}_3\text{O}_4\text{-TiO}_2/\text{Ti}$ (c); Cyclic voltammograms obtained with $\text{Co}_3\text{O}_4\text{-TiO}_2/\text{Ti}$ cathode (d) in 0.1 M SO_4^{2-} in the presence (dotted line) and absence (full line) of 10 mM TBA ; LSV curves of different electrolyte (e); and concentration decay kinetics of NO_3^- at $\text{Co}_3\text{O}_4\text{-TiO}_2/\text{Ti}$ cathode (f) with various TBA concentrations (Experimental conditions: $[\text{NO}_3^-]_0 = 50 \text{ mg L}^{-1}$, $\text{pH} = 7.0$, current density = 10 mA cm^{-2}).

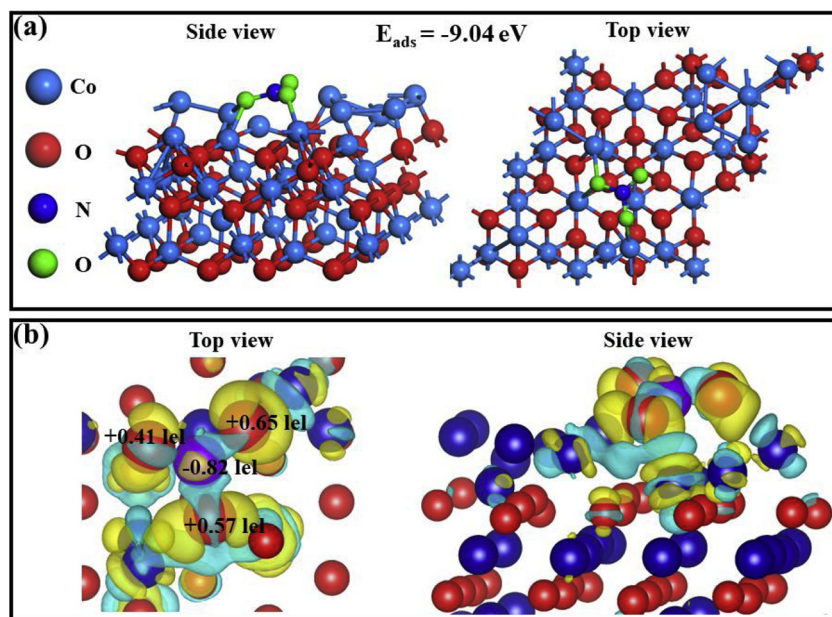
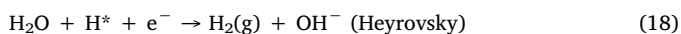
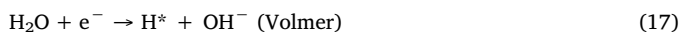


Fig. 11. (a) Adsorption configuration of NO_3^- on Co_3O_4 (222) surface and corresponding adsorption energy, (b) Differential charge density distribution of NO_3^- on Co_3O_4 (222) surface. Electron accumulation and electron deletion are represented by yellow and blue, respectively (For interpretation of the references to colour in this figure legend, the reader is referred to the web version of this article).

addition of 5 and 50 mg L^{-1} NO_3^- . However, the current intensity was decreased as TBA was added, which was more pronounced at higher TBA concentration. In addition, as shown in Fig. 10(f), increasing TBA concentration could gradually inhibit the NO_3^- removal efficiency. When TBA concentration was 0.2 mM, the NO_3^- removal efficiency was decreased by approximately 10%, and it was further decreased by 18% at TBA concentration of 1 mM. But negligible difference in the NO_3^- reduction efficiency between 1 and 10 mM TBA was observed, suggesting nearly complete hindering of the contribution of the formed H^* to NO_3^- reduction when TBA concentration was 1 mM. Therefore, we can reasonably speculate that approximately 18% NO_3^- reduction proceeded via the indirect pathway mediated by the atomic H^* during the electrocatalytic reduction of NO_3^- process.

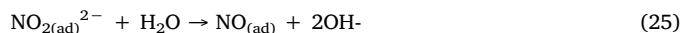
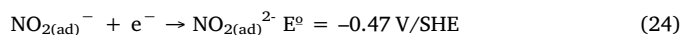
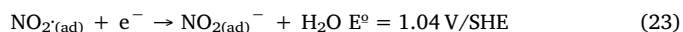
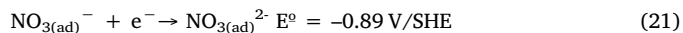
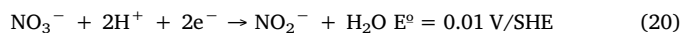
Atomic H^* would accordingly be generated first by Volmer mechanism (Eq. (17)), which can explain the increase of solution pH observed for the Co_3O_4 - TiO_2 -PVP cathode. In some noble metal catalysts (e.g., Pd and Ag)-based reaction systems, atomic H^* would be favorably preserved for NO_3^- reduction [12]. As a result, after the addition of 1 mM and 10 mM TBA in the Pd-mediated process, the NO_3^- removal rate constant was reduced by 38% and 81%, respectively, which fully demonstrates the importance of atomic H^* for NO_3^- reduction. For Pd-based catalysts, the high efficiency of the use of protons to generate atomic H^* at low overpotentials (Eq. (17)) and the strong adsorption of atomic H^* to Pd atoms make Eqs. (18) and (19) difficult to occur [47,48]. Even if atomic H^* is converted to H_2 , Pd atoms can cleave H_2 and regenerate atomic H^* (this mechanism belongs to catalytic reduction) [12]. Through such electrocatalytic reduction processes, the indirect reduction of NO_3^- by Pd-based catalysts is dominant. In contrast, in present Co_3O_4 -based electrochemical system, the produced H^* was inclined to transform to H_2 by Heyrovsky and Tafel routes (Eqs. (17)–(19)) [15]. Consequently, as for Co_3O_4 - TiO_2 -PVP cathode, the indirect reduction mediated by atomic H^* accounted for only 18% of NO_3^- reduction. Thus, the role of atomic H^* in the electrocatalytic reduction of NO_3^- at the Co_3O_4 - TiO_2 -PVP electrode was secondary, while the direct electron transfer was mainly responsible for NO_3^- reduction. In view of this, future research should focus on improving the atomic H^* adsorption capacity of non-precious metal catalysts.



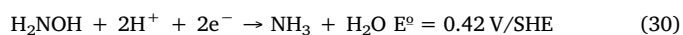
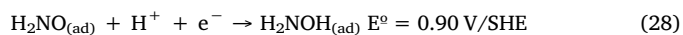
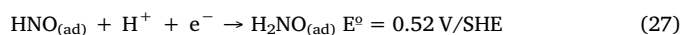
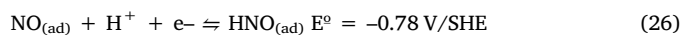
3.4.3. Proposed reaction pathway

It was observed from Fig. 1 that the NH_4^+ concentration gradually increased over the reaction time for all cathodes containing Co_3O_4 catalyst as it was the main product of electrocatalytic NO_3^- reduction, while NO_2^- was the minor intermediate product at a relatively low concentration. According to the aforementioned discussion and the experimental results, there are two main pathways (i.e., Co-mediated direct reduction and atomic H^* -mediated indirect reduction) responsible for the electrocatalytic reduction of NO_3^- by the Co_3O_4 bearing cathodes investigated in this study.

It is known that the reduction of NO_3^- to NO_2^- (Eq. (20)) is the kinetically rate-determining step for the electrocatalytic reduction of NO_3^- . This step actually consists of the reactions set presented through Eqs. (21)–(23) which is known as an electrochemical-chemical-electrochemical path [35]. The elementary electron transfer reactions lead to the generation of $\text{NO}_3^{\cdot-}(\text{ad})$ and $\text{NO}_2^{\cdot-}(\text{ad})$, which are adsorbed short-lived intermediates. Then, $\text{NO}_2^{\cdot-}(\text{ad})$ converts to an unstable dianion radical, namely $\text{NO}_2^{2-}(\text{ad})$, by direct electron transfer (Eq. (24)), which would quickly hydrolyzes to form $\text{NO}(\text{ad})$ (Eq. (25)) [35]:



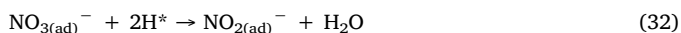
According to the previous studies, the stepwise reduction of $\text{NO}(\text{ad})$ eventually forms NH_4^+ , which is regarded as an electrochemical-electrochemical path, as depicted in Eqs. (26)–(31) [49]:





The direct electron transfers in above reactions are mostly single electron transfer processes. The above experimental results demonstrated that the redox process $\text{Co}^{2+} \rightarrow \text{Co}^{3+} \rightarrow \text{Co}^{2+}$ accelerates the electron transfer during NO_3^- reduction. The source of electrons for NO_3^- reduction is directly derived from Co^{2+} instead of the cathode through the circuit. Co^{2+} gives an electron to NO_3^- or its daughter intermediates with the formation of Co^{3+} , and then Co^{3+} would transform to Co^{2+} via obtaining an electron from the cathode surface. Thus, during the whole reaction, Co_3O_4 mainly acts as an electron shuttle rather than a reducing agent. Moreover, H^+ is consumed in many NO_3^- reduction steps, which is consistent with the pH variation as shown in Fig. 7(b).

At the same time, due to the strong reducibility of atomic hydrogen ($E_{(\text{H}^+/\text{H})} = -2.31 \text{ V/SHE}$) [49], the indirect reduction path of NO_3^- can not be ignored. Atomic H^* involved in Eqs. (32)–(37).



4. Conclusions

A novel $\text{Co}_3\text{O}_4\text{-TiO}_2/\text{Ti}$ cathode was synthesized for removal of NO_3^- from water by its electrocatalytic reduction of. It was proved that adding a certain amount of PVP in the coating liquid could improve the dispersibility of the catalyst and therefore promote the electrocatalytic reduction of NO_3^- . More importantly, the release of toxic Co ions into the solution was almost completely prohibited during the NO_3^- reduction process due to the stabilization effect of TiO_2 . The introduction of a certain amount of chloride ions into the electrolyte significantly increased the N_2 selectivity and total nitrogen removal efficiency. When the concentration of chloride ions reached 2000 mg L^{-1} , almost no NH_4^+ was detected after 100 min of electrolysis. The electrocatalytic mechanism of NO_3^- reduction consisted of direct reduction and indirect reduction, which are mediated by the $\text{Co}^{2+} \rightarrow \text{Co}^{3+} \rightarrow \text{Co}^{2+}$ redox cycle and atomic H^* , respectively. Notably, the former route played a superior role in NO_3^- reduction over the latter one. Generally, considering the abundant chloride ions in industrial/municipal wastewaters, the developed $\text{Co}_3\text{O}_4\text{-TiO}_2/\text{Ti}$ cathode in this study might be a promising alternative for the electrocatalytic treatment of aqueous effluents loaded with NO_3^- .

Acknowledgments

This work is financially supported by the National Natural Science Foundation of China (No. 51608284, 41775119), National Major Science and Technology Program for Water Pollution Control and Treatment (No. 2017ZX07101-006), China Postdoctoral Science Foundation (No. 2017M610413), Shandong Province Postdoctoral Science Foundation (No. 201702041).

Appendix A. Supplementary data

Supplementary material related to this article can be found, in the online version, at doi:<https://doi.org/10.1016/j.apcatb.2019.05.016>.

References

- [1] X. Huo, D.J.V. Hoomissen, J. Liu, S. Vyas, T.J. Strathmann, Hydrogenation of aqueous nitrate and nitrite with ruthenium catalysts, *Appl. Catal. B: Environ.* 211 (2017) 188–198.
- [2] Z. Hou, F. Chen, J. Wang, C.P. François-Xavier, T. Wintgens, Novel Pd/GdCrO₃ composite for photo-catalytic reduction of nitrate to N₂ with high selectivity and activity, *Appl. Catal. B: Environ.* 232 (2018) 124–134.
- [3] Q. Song, M. Li, L. Wang, X. Ma, F. Liu, X. Liu, Mechanism and optimization of electrochemical system for simultaneous removal of nitrate and ammonia, *J. Hazard. Mater.* 363 (2019) 119–126.
- [4] Z. Gao, Y. Zhang, D. Li, C.J. Werth, Y. Zhang, X. Zhou, Highly active Pd-In/mesoporous alumina catalyst for nitrate reduction, *J. Hazard. Mater.* 286 (2015) 425–431.
- [5] M. Duca, N. Sacré, A. Wang, S. Garbarino, D. Guay, Enhanced electrocatalytic nitrate reduction by preferentially-oriented (100) PtRh and PtIr alloys: the hidden treasures of the ‘miscibility gap’, *Appl. Catal. B: Environ.* 221 (2018) 86–96.
- [6] S.K. Sharma, R.C. Soti, Nitrate removal from ground water: a review, *J. Chem.* 9 (2012) 1667–1675.
- [7] E. Lacasa, P. Cañizares, C. Sáez, F.J. Fernández, M.A. Rodrigo, Removal of nitrates from groundwater by electrocoagulation, *Chem. Eng. J.* 171 (2011) 1012–1017.
- [8] A.P. Murphy, Chemical removal of nitrate from water, *Nature* 350 (1991) 223.
- [9] M. Kumar, S. Chakraborty, Chemical denitrification of water by zero-valent magnesium powder, *J. Hazard. Mater.* 135 (2006) 112–121.
- [10] H. Kominami, T. Nakaseko, Y. Shimada, A. Furusho, H. Inoue, S.Y. Murakami, Y. Kera, B. Ohtani, Selective photocatalytic reduction of nitrate to nitrogen molecules in an aqueous suspension of metal-loaded titanium(IV) oxide particles, *Chem. Commun.* 23 (2005) 2933–2935.
- [11] Y. Yoshinaga, T. Akita, I. Mikami, T. Okuhara, Hydrogenation of nitrate in water to nitrogen over Pd–Cu supported on active carbon, *J. Catal.* 207 (2002) 37–45.
- [12] J. Martinez, A. Ortiz, I. Ortiz, State-of-the-art and perspectives of the catalytic and electrocatalytic reduction of aqueous nitrates, *Appl. Catal. B: Environ.* 207 (2017) 42–59.
- [13] U. Prüsse, M. Hähnlein, J. Daum, K.D. Vorlop, Improving the catalytic nitrate reduction, *Catal. Today* 55 (2000) 79–90.
- [14] B.P. Dash, S. Chaudhari, Electrochemical denitrification of simulated ground water, *Water Res.* 39 (2005) 4065–4072.
- [15] M.G. de Chialvo, A. Chialvo, Kinetics of hydrogen evolution reaction with Frumkin adsorption: re-examination of the Volmer–Heyrovsky and Volmer–Tafel routes, *Electrochim. Acta* 44 (1998) 841–851.
- [16] B.P. Chaplin, M. Reinhard, W.F. Schneider, C. Schüth, J.R. Shapley, T.J. Strathmann, C.J. Werth, Critical review of Pd-based catalytic treatment of priority contaminants in water, *Environ. Sci. Technol.* 46 (2012) 3655–3670.
- [17] X. Zhou, Z. Liu, Y. Wang, Y. Ding, Facet effect of Co₃O₄ nanocrystals on visible-light driven water oxidation, *Appl. Catal. B: Environ.* 237 (2018) 74–84.
- [18] S. Gao, X. Jiao, Z. Sun, W. Zhang, Y. Sun, C. Wang, Q. Hu, X. Zu, F. Yang, S. Yang, Ultrathin Co₃O₄ layers realizing optimized CO₂ electroreduction to formate, *Angew. Chem. Int. Ed.* 55 (2016) 698–702.
- [19] B. Meng, Z. Zhao, X. Wang, J. Liang, J. Qiu, Selective catalytic reduction of nitrogen oxides by ammonia over Co₃O₄ nanocrystals with different shapes, *Appl. Catal. B: Environ.* 129 (2013) 491–500.
- [20] L. Su, K. Li, H. Zhang, M. Fan, D. Ying, T. Sun, Y. Wang, J. Jia, Electrochemical nitrate reduction by using a novel Co₃O₄/Ti cathode, *Water Res.* 120 (2017) 1–11.
- [21] W. Teng, N. Bai, Y. Liu, Y. Liu, J. Fan, W.X. Zhang, Selective nitrate reduction to dinitrogen by electrocatalysis on nanoscale iron encapsulated in mesoporous carbon, *Environ. Sci. Technol.* 52 (2017) 230–236.
- [22] G.M. Tomboc, F.O. Agyemang, H. Kim, Improved electrocatalytic oxygen evolution reaction properties using PVP modified direct growth Co-based metal oxides electrocatalysts on nickel foam, *Electrochim. Acta* 263 (2018) 362–372.
- [23] Z. Dasgelen, Y. Yildiz, S. Eris, F. Şen, Enhanced electrocatalytic activity and durability of Pt nanoparticles decorated on GO-PVP hybrid material for methanol oxidation reaction, *Appl. Catal. B: Environ.* 219 (2017) 511–516.
- [24] H. Tsunoyama, T. Tsukuda, Magic numbers of gold clusters stabilized by PVP, *J. Am. Chem. Soc.* 131 (2009) 18216–18217.
- [25] J. Yu, J. Xiong, B. Cheng, S. Liu, Fabrication and characterization of Ag–TiO₂ multiphase nanocomposite thin films with enhanced photocatalytic activity, *Appl. Catal. B: Environ.* 60 (2005) 211–221.
- [26] H. Yue, L. Xue, F. Chen, Efficient electrochemical removal of nitrite contamination with stable RuO₂-TiO₂/Ti electrodes, *Appl. Catal. B: Environ.* 206 (2017) 683–691.
- [27] T. Hong, Z. Liu, X. Zheng, J. Zhang, L. Yan, Efficient photoelectrochemical water splitting over Co₃O₄ and Co₃O₄/Ag composite structure, *Appl. Catal. B: Environ.* 202 (2017) 454–459.
- [28] J. Yu, B. Wang, Effect of calcination temperature on morphology and photoelectrochemical properties of anodized titanium dioxide nanotube arrays, *Appl. Catal. B: Environ.* 94 (2010) 295–302.
- [29] Y. Ren, J. Yang, J. Li, B. Lai, Strengthening the reactivity of Fe⁰/(Fe/Cu) by pre-magnetization: Implications for nitrate reduction rate and selectivity, *Chem. Eng. J.* 330 (2017) 813–822.
- [30] C. Zhang, D. He, J. Ma, T.D. Waite, Active chlorine mediated ammonia oxidation revisited: reaction mechanism, kinetic modelling and implications, *Water Res.* 145 (2018) 220–230.
- [31] T.A. Pressley, D.F. Bishop, S.G. Roan, Ammonia-nitrogen removal by breakpoint chlorination, *Environ. Sci. Technol.* 6 (1972) 622–628.
- [32] Z. Qiang, C.D. Adams, Determination of monochloramine formation rate constants

- with stopped-flow spectrophotometry, *Environ. Sci. Technol.* 38 (2004) 1435–1444.
- [33] L. Li, Y. Liu, Ammonia removal in electrochemical oxidation: mechanism and pseudo-kinetics, *J. Hazard. Mater.* 161 (2009) 1010–1016.
- [34] J. Ding, Q. Zhao, Y. Zhang, L. Wei, W. Li, K. Wang, The eAND process: enabling simultaneous nitrogen-removal and disinfection for WWTP effluent, *Water Res.* 74 (2015) 122–131.
- [35] S. Garcia-Segura, M. Lanzarini-Lopes, K. Hristovski, P. Westerhoff, Electrocatalytic reduction of nitrate: fundamentals to full-scale water treatment applications, *Appl. Catal. B: Environ.* 236 (2018) 546–568.
- [36] M. Hasnat, S.B. Aoun, S.N. Uddin, M.M. Alam, P. Koay, S. Amertharaj, M. Rashed, M.M. Rahman, N. Mohamed, Copper-immobilized platinum electrocatalyst for the effective reduction of nitrate in a low conductive medium: mechanism, adsorption thermodynamics and stability, *Appl. Catal. A Gen.* 478 (2014) 259–266.
- [37] J.F. Su, I. Ruzybayev, I. Shah, C.P. Huang, The electrochemical reduction of nitrate over micro-architected metal electrodes with stainless steel scaffold, *Appl. Catal. B: Environ.* 180 (2016) 199–209.
- [38] J. Heinze, Cyclic voltammetry—“electrochemical spectroscopy”. *New analytical methods* (25), *Angew. Chem. Int. Ed. Engl.* 23 (1984) 831–847.
- [39] A. Li, X. Zhao, Y. Hou, H. Liu, L. Wu, J. Qu, The electrocatalytic dechlorination of chloroacetic acids at electrodeposited Pd/Fe-modified carbon paper electrode, *Appl. Catal. B: Environ.* 111 (2012) 628–635.
- [40] C. Liu, A.Y. Zhang, D.N. Pei, H.Q. Yu, Efficient electrochemical reduction of nitrobenzene by defect-engineered TiO_{2-x} single crystals, *Environ. Sci. Technol.* 50 (2016) 5234–5242.
- [41] Y. Liu, R. Luo, Y. Li, J. Qi, C. Wang, J. Li, X. Sun, L. Wang, Sandwich-like $\text{Co}_3\text{O}_4/\text{MXene}$ composite with enhanced catalytic performance for Bisphenol A degradation, *Chem. Eng. J.* 347 (2018) 731–740.
- [42] X. Qiu, J. Yu, H. Xu, W. Chen, W. Hu, G. Chen, Interfacial effects of the Cu_2O nanodots decorated Co_3O_4 nanorods array and its photocatalytic activity for cleaving organic molecules, *Appl. Surf. Sci.* 382 (2016) 249–259.
- [43] M. Kang, M.W. Song, C.H. Lee, Catalytic carbon monoxide oxidation over $\text{CoO}_x/\text{CeO}_2$ composite catalysts, *Appl. Catal. A Gen.* 251 (2003) 143–156.
- [44] K.Y.A. Lin, B.C. Chen, Efficient elimination of caffeine from water using Oxone activated by a magnetic and recyclable cobalt/carbon nanocomposite derived from ZIF-67, *Dalton Trans.* 45 (2016) 3541–3551.
- [45] J. Li, G. Lu, G. Wu, D. Mao, Y. Guo, Y. Wang, Y. Guo, Effect of TiO_2 crystal structure on the catalytic performance of $\text{Co}_3\text{O}_4/\text{TiO}_2$ catalyst for low-temperature CO oxidation, *Catal. Sci. Technol.* 4 (2014) 1268–1275.
- [46] G. Jiang, M. Lan, Z. Zhang, X. Lv, Z. Lou, X. Xu, F. Dong, S. Zhang, Identification of active hydrogen species on palladium nanoparticles for an enhanced electrocatalytic hydrodechlorination of 2, 4-dichlorophenol in water, *Environ. Sci. Technol.* 51 (2017) 7599–7605.
- [47] R. Liu, H. Zhao, X. Zhao, Z. He, Y. Lai, W. Shan, D. Bekana, G. Li, J. Liu, Defect sites in ultrathin Pd nanowires facilitate the highly efficient electrochemical hydrodechlorination of pollutants by H_{ads}^+ , *Environ. Sci. Technol.* 52 (2018) 9992–10002.
- [48] B. Jiang, Y. Gong, J. Gao, T. Sun, Y. Liu, N. Oturan, M.A. Oturan, Reductive detoxification of Cr (VI) mediated by environmentally relevant carboxylic acids: state-of-the-art and perspectives, *J. Hazard. Mater.* 365 (2018) 205–226.
- [49] A. De Vooy, M. Koper, R. Van Santen, J. Van Veen, The role of adsorbates in the electrochemical oxidation of ammonia on noble and transition metal electrodes, *J. Electroanal. Chem.* 506 (2001) 127–137.